

Simulating spectroscopy experiments with a superconducting quantum computer

John P. T. Stenger,¹ Gilad Ben-Shach¹,² David Pekker¹,³ and Nicholas T. Bronn¹^{4,*}

¹*U.S. Naval Research Laboratory, Washington, DC 20375, USA*

²*IBM Quantum, IBM Canada, Markham, Ontario, Canada L6G 1C7*

³*Department of Physics and Astronomy, University of Pittsburgh, Pittsburgh, Pennsylvania 15260, USA*

⁴*IBM Quantum, IBM T. J. Watson Research Center, Yorktown Heights, New York 10598, USA*



(Received 28 February 2022; revised 15 July 2022; accepted 12 October 2022; published 15 November 2022)

We present a method for solving eigenvalue problems on a quantum computer based on spectroscopy. The method works by coupling a “probe” qubit to a set of system simulation qubits and then time evolving both the probe and the system under Hamiltonian dynamics. In this way, we simulate spectroscopy on a quantum computer. We test our method on the IBM quantum hardware for a simple single-spin model and an interacting Kitaev chain model. For the Kitaev chain, we trace out the pseudotopological phase boundary for a two-site model.

DOI: [10.1103/PhysRevResearch.4.043106](https://doi.org/10.1103/PhysRevResearch.4.043106)

I. INTRODUCTION

The simulation of quantum systems with a quantum computer was originally proposed by Feynman [1], which sparked the nascent field. While the dynamics of quantum systems are fully determined (e.g., by the Schrödinger equation), the dimension of the Hilbert space that describes their evolution scales exponentially in the number of degrees of freedom, which makes classical calculations impossible for a large enough system size. The recent availability of quantum computers in the cloud allows practitioners to begin to map problems of quantum simulation and achieve proof-of-principle results [2–7], even starting to surpass the accuracy of state-of-the-art classical approximations [8]. While quantum phase estimation (QPE) [9] offers an exponential speedup in determining Hamiltonian spectra, it requires a depth of circuit unfeasible for near-term noisy quantum hardware. Short-depth hybrid algorithms such as the variational quantum eigensolver (VQE) are amenable to current hardware at the expense of many iterations over measurements and optimization cycles [10–16]. Furthermore, VQE requires a problem-specific ansatz which is not generalizable to all systems. Here we propose a spectroscopic eigensolver method which makes efficient use of available noisy near-term quantum resources. Our method is both amenable to noisy quantum hardware and generally applicable to determining Hamiltonian spectra.

II. THE SPECTROSCOPIC EIGENSOLVER

We present a quantum eigensolver method which is akin to the experimental tool of tunneling spectroscopy. Our method involves a “probe qubit” and a “simulation” register that undergo Hamiltonian evolution for a time t . A cartoon of our method is depicted in Fig. 1(a). Measurement of the probe qubit q_0 reveals the spectrum of the evolved Hamiltonian via its response when the probe energy is on resonance with an energy transition in the system, schematically shown as a dip in Fig. 1(b). While similar to other time-evolution algorithms [9,17], this technique does not require controlled-coherent evolution of the register by auxiliary qubits. Instead, the probe qubit evolving according to an energy (via ω) interacts transversely with a single qubit of the simulation register. This process is repeated over a number of Trotter steps, as shown in Fig. 1(c). We have the freedom to select the specific qubit being probed. It is only necessary that the wave function of the simulation register has strong weight on that qubit. This method is conducive for execution on near-term noisy quantum hardware because it requires only a local interaction between qubits instead of the controlled evolution of an entire simulation register, substantially reducing circuit depth because no SWAP operations are necessary between the probe qubit and simulation register, and naturally maps to the planar architecture of current superconducting quantum hardware (see Appendix A). Furthermore, only measurement of the probe qubit is required, reducing readout error. The underlying trade-off compared to other algorithms is the number of circuits that must be executed: one for each value of ω , a sweep of which is required for accurate fitting and hence determination of the eigenvalues (see Appendix B). However, recent improvements as determined by speed benchmarking show this is not a bottleneck for superconducting quantum hardware [18].

Explicitly, the spectroscopic eigensolver technique finds the energy differences of a system by coupling a probe qubit to a Pauli Hamiltonian H_{Pauli} suitably encoded to enforce

*Corresponding author: ntbronn@us.ibm.com

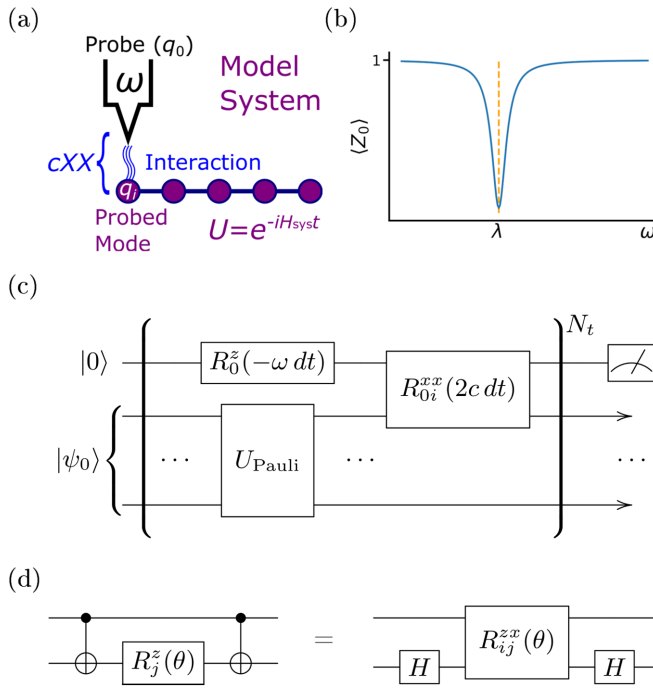


FIG. 1. Quantum circuits for simulating the time evolution $U_{\text{Pauli}} = e^{-iH_{\text{Pauli}}t}$: (a) a cartoon analogy of the spectroscopy eigen-solver method to scanning tunneling spectroscopy, where a tip (qubit) at potential (energy) ω interacts with a single mode of a model system via electron tunneling (transverse cXX interaction), revealing (b) a response as a function of energy which determines an eigenvalue λ as a dip in probe expectation $\langle Z_0 \rangle$. (c) The spectroscopic eigen-solver algorithm for a probe qubit interacting with a single qubit of the simulation register (for N_t Trotter steps U_{res} , first order shown for clarity) followed by measurement of the probe qubit and (d) a circuit equivalence that allows efficient implementation of scaled pulses with the native $R^{zx}(\theta)$ interaction generated by echoed cross resonance [20].

the commutation relations of the system Hamiltonian H_{sys} it represents. The full Hamiltonian, which we will refer to as the “resonance” Hamiltonian because of its response when the probe and system are on resonance, is

$$H_{\text{res}} = -\frac{1}{2}\omega Z_0 + cX_0X_i + H_{\text{Pauli}}, \quad (1)$$

where the probe qubit q_0 with energy ω is at index 0, c is the coupling parameter between the probe and probed qubit q_i of the simulated system, and the tensor products with identity matrices are omitted for succinctness. The first-order Suzuki-Trotter decomposition of the time-evolution unitary is

$$U_{\text{res}}(\omega, dt) = e^{-iH_{\text{res}}dt} \approx R_{0i}^{xx}(2c dt)R_0^z(-\omega dt)U_{\text{Pauli}}, \quad (2)$$

where $R_j^z(\phi)$ is a Z rotation on site j , $R_{jk}^{xx}(\theta)$ is an XX rotation on sites j and k , and $U_{\text{Pauli}} = e^{-iH_{\text{Pauli}}dt}$ is the Trotter step of time evolution $dt = t/N_t$ for the system.

We start in state $|0, \psi_0\rangle$ with the probe qubit in the ground state and the system $|\psi_0\rangle$ in an arbitrary state. For simplicity we will take $|\psi_0\rangle$ to be the n -qubit ground state. After N_t applications of U_{res} , we measure the probe qubit in the Z basis, $\langle Z_0 \rangle(\omega) = \langle 0, \psi_0 | (U_{\text{res}}^\dagger)^{N_t} Z_0 U_{\text{res}}^{N_t} | 0, \psi_0 \rangle$. When c is small compared to the energy scales in H_{Pauli} and when ω is on

resonance with an energy transition of H_{Pauli} , the probability of the probe qubit flipping will peak, resulting in a dip in $\langle Z_0 \rangle(\omega)$.

III. EXPERIMENTAL METHODS

The following experiments were conducted within the QISKit [19] framework with jobs sent to the cloud-based IBM Lagos, a seven-qubit superconducting IBM Quantum backend. First, the system Hamiltonian is mapped to a qubit (Pauli) Hamiltonian by a suitable encoding. The Pauli Hamiltonian is then mapped to unitary time evolution via the second-order Suzuki-Trotter transformation. The resulting circuit consists of two-qubit rotations on the order of $c dt$, ωdt , etc., where the digital synthesis of each is locally equivalent to a Z rotation sandwiched by two CNOTs, which is more efficiently implemented by scaled gates that rotate smaller angles in the two-qubit Hilbert space natively [the equivalence of which is shown in Fig. 1(d)] instead of the (net) two-qubit π rotation in the former case [2]. These scaled pulses are implemented as calibrations for $R^{zx}(\theta)$ gates [20] following an analysis of the circuit using a template optimization technique [21]. Each spectroscopic experiment is then built as an array of circuits, one for each value of ω . For each circuit, a result consisting of the measurement strings of 8192 shots is returned and analyzed. This allows us to find the energy transitions by locating dips in $\langle Z_0 \rangle(\omega)$. Further details are provided in the Appendixes, and full data and the source code can be found in Ref. [22].

IV. APPLICATION I: LANDAU-ZENER MODEL

As a first test case, we take the system to be a single spin under two opposing magnetic fields,

$$H_{\text{Pauli}} = H_{\text{sys}} = aZ_1 + bY_1. \quad (3)$$

We treat b as fixed and vary a so that the energy levels form an avoided crossing. Both a and b are treated as unitless algorithmic quantities. In Fig. 2 we show scans of the orientation of the probe qubit $\langle Z_0 \rangle(\omega)$ for several values of a . Notice that there is a dip at $\omega = 0$. This corresponds to the transition of an energy level to itself; see Appendix C for details.

We find excellent agreement between the exact energy transitions and the local minimum in $\langle Z_0 \rangle(\omega)$. The root-mean-square (rms) of the variance of all three transitions together is $\text{rms} = \sqrt{\frac{1}{N_d} \sum_{i=0}^{N_d} (\omega_i^* - \Delta E_i)^2} \approx 0.083$, where N_d is the number of data points, ω_i^* is a minimum, and ΔE_i is the corresponding energy transition. The rms variance is about an order of magnitude less than the average uncertainty calculated from the full width-at half minimum (FWHM), which includes both hardware and Trotter error, $\text{FWHM} = \frac{1}{N_d} \sum_{i=0}^{N_d} (\omega_i^L - \omega_i^R) \approx 0.811$, where ω_i^L is the value of ω when $\langle Z_0 \rangle(\omega)$ is half way between its minimum and maximum value to the left of ω_i^* and ω_i^R is the same but to the right of ω_i^* . This simple test system stands to demonstrate how accurate our algorithm can be when the decoherence time of the qubits (~ 100 – 150 μ s) allows for a long evolution time $t \gg dt$, where t corresponds to ~ 15 μ s of hardware time for this example. With this in mind, we will push our algorithm

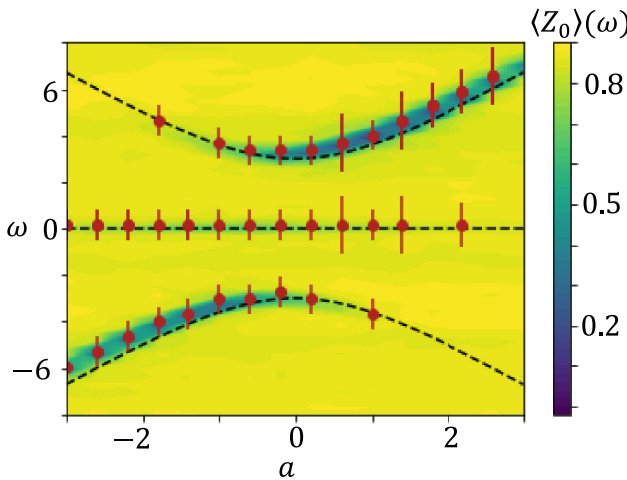


FIG. 2. Scans of the probe qubit expectation value as a function of ω for many values of a . The minimums in $\langle Z_0 \rangle(\omega)$ for each value of a are plotted as red circles. The error bars represent the full width at half minimum for the $\langle Z_0 \rangle(\omega)$ dips. The black dashed lines are the expected value of the energy transitions as obtained from exact diagonalization. The parameter values are $c = 0.1$, $t = 10$, $dt = 0.3\bar{3}$.

to the limits of the quantum hardware by testing a more complicated system.

V. APPLICATION II: TWO-SITE KITAEV CHAIN

A system of particular interest in tunneling spectroscopy is the n -site Kitaev chain which hosts Majorana zero modes (MZMs) in the topological regime. The Kitaev chain is a particularly good test case for the spectroscopic eigensolver technique since the MZMs exist at the ends of the chain and are therefore easy to probe. Distinguishing the topological phase from the trivial superconducting phase in such nanowires has been a recent theoretical interest largely motivated by the fact that Majorana zero modes promise application in topologically protected quantum computation [23–28]. The topological regime is characterized by a change in parity of the ground state. While the topological regime is truly present only in an $n \rightarrow \infty$ limit, a parity flip occurs even in a two-site model.

The model Hamiltonian of the interacting Kitaev chain with Coulomb interactions is

$$H_{\text{sys}} = \mu \sum_{i=1}^L c_i^\dagger c_i + g \sum_{i=1}^{L-1} (c_i^\dagger c_{i+1} + c_{i+1}^\dagger c_i) + \Delta \sum_{i=1}^{L-1} (c_i^\dagger c_{i+1}^\dagger + c_{i+1} c_i) + V \sum_{i=1}^{L-1} c_i^\dagger c_i c_{i+1}^\dagger c_{i+1}, \quad (4)$$

where L is the number of sites, c_i^\dagger (c_i) is the creation (annihilation) operator on site i , μ is the chemical potential, g is the hopping rate, Δ controls the superconductivity pairing strength, and V is the interaction strength. The inclusion of the interaction term makes the system difficult to study classically but poses no additional fundamental challenges for quantum processors [29,30].

Using the Jordan-Wigner encoding [17], we can express Eq. (4) as

$$H_{\text{Pauli}} = x \sum_{i=1}^{n-1} X_i X_{i+1} + y \sum_{i=1}^{n-1} Y_i Y_{i+1} + z \sum_{i=1}^{n-1} Z_i Z_{i+1} - m \sum_{i=1}^n Z_i - \bar{m} \sum_{i=2}^{n-1} Z_i, \quad (5)$$

where X_i , Y_i , and Z_i are Pauli matrices acting on qubit i , $n = L$ is the number of qubits used to represent the system, and $2x = g + \Delta$, $2y = g - \Delta$, $4z = V$, $4m = 2\mu + V$, and $4\bar{m} = V$. These parameters are considered to be unitless algorithmic quantities; however, the values we will use roughly correspond to those of real systems if they are taken to be in the meV range [31].

In the limit $n \rightarrow \infty$, this system has a topological phase transition in parameter space. We will restrict ourselves to the two-site $n = 2$ model in the main text. See Appendix F for an explanation of how to relate the two-site model and the $n \rightarrow \infty$ limit, and see Appendix H for experimental results for the $n = 3$ model. In the $n = 2$ case the gap between the ground and first excited states closes along the surface

$$m = \sqrt{z^2 + z(x+y) + xy}; \quad (6)$$

see Appendix G for details. This surface can be thought of as a remnant of the topological phase boundary. We now explore the use of the spectroscopic eigensolver technique to analyze this surface.

Because the circuit depth is long in this case, it is important that we optimize the parameters. We optimized the time t , time step dt , and coupling c (see Appendix D). In Fig. 3(a) we show a sweep of the probe qubit's energy ω for three values of c . The energy difference between the ground and first excited states is determined by the ω at which $\langle Z_0 \rangle(\omega)$ is minimum. When c is too low, the probe qubit will not respond to the system, but if c is too high, it will perturb the system. Note the state transition from the ground to first excited state (denoted by the notation $[0,1]$) is visible in Fig. 3(a) but the reverse transition is not. This is due to the initial state of the system qubits, set to $|00\rangle$ for simplicity, which has no overlap with the odd parity excited state, so only the forward transition is possible. Considering a single parity in this way allows maximum contrast in our signal. Absent also is the $\omega = 0$ dip, which is true for all fermionic Hamiltonians (see Appendix C), making them particularly amenable to our method. At the edges of Fig. 3(a) we see the onset of higher energy transitions.

Scans of $\langle Z_0 \rangle(\omega)$ for several values of y are shown in Figs. 3(b) and 3(c). In Fig. 3(b) the locations of all local minima are displayed. In Fig. 3(c) we isolate the $[0,1]$ transition by locating the minimum which is closest to $\omega = 0$ [circled in yellow in Fig. 3(b)] and then track the dip by going to the neighboring values of y and finding the minimum which is closest to the last one. The average FWHM ≈ 2.35 is larger than the separation of some energy transitions. This can cause dips from two different energy transitions to merge into one, shifting the location of the dip. Even with this concern, we get fairly accurate results. The rms variance ≈ 1.72 for the $[0,1]$ transition, which is well within the width of the peak.

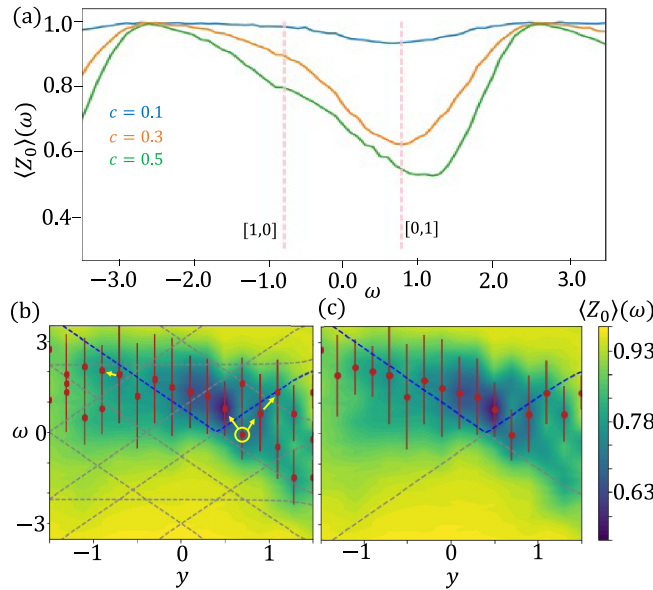


FIG. 3. Scans of the probe qubit expectation value as a function of ω . (a) Sweeps of the probe qubit frequency for different values of c . For these sweeps, $m = 1.0$, $x = 1.5$, $y = 0.4$, $z = 0.2$, $dt = 0.7$, and $t = 5$. The vertical lines are the expected transitions from the classical solution. For more c sweeps, see Appendix D. (b) and (c) Sweeps of the probe qubit frequency for different values of y . For these sweeps, $c = 0.3$, $m = 0.1$, $x = 1.5$, $z = 0.4$, $dt = 0.7$, and $t = 5$. The minimums in $\langle Z_0 \rangle(\omega)$ for each value of y are plotted as red circles. The error bars represent the half width at half minimum for the $\langle Z_0 \rangle(\omega)$ dips. The blue dashed line represents the $[0,1]$ transition, while other transitions are in gray. In (b) we show all transitions and all local minimums of $\langle Z_0 \rangle(\omega)$. In (c) we show only the $[0,1]$ and $[1,0]$ transitions, and we select the minimums by tracking as depicted by the yellow arrow in (b).

Taking several scans of ω for different values of m and y , we are able to trace out the pseudophase boundary. Figures 4(a) and 4(b) show the absolute value of the gap for a classical simulation without noise and the results from the

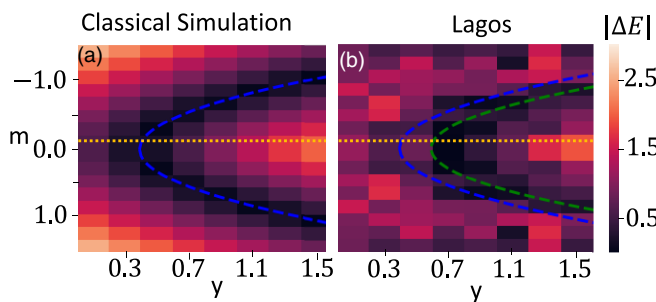


FIG. 4. Energy difference between the ground and first excited states as a function of m and y . (a) Simulation on a classical computer with no error. (b) Results from the IBM Lagos backend. In both plots, $c = 0.3$, $x = 1.5$, $z = 0.4$, $dt = 0.7$, and $t = 5.0$. In both panels, the orange line shows the location of the data in Figs. 3(b) and 3(c), and the blue curve is the expected zero crossing from Eq. (6) with the above parameters. The green curve in (b) is the zero crossing, again using Eq. (6) with z as the free parameter. We find the best fit z is shifted by $\Delta z = 0.19$.

quantum device, respectively. The curve of points at which the gap goes to zero is the phase boundary. Notice that in the results from the quantum device the boundary is pushed to higher values of y than in the perfect simulation. The green line is a best fit of the boundary to Eq. (6) with z as the fit parameter. We find a shift of $\Delta z = 0.19$ which is well within the average FWHM ≈ 2.35 found above. Using the best fit z , we find that the shape of the boundary is fairly accurate with rms ≈ 0.15 , which is again well within the average FWHM. The error is largely due to the width of the $\langle Z_0 \rangle(\omega)$ dips and the influence of nearby transitions. As seen in Fig. 3 the $[0,1]$ dip is pulled to higher ω by the $[2,3]$ transition near the phase boundary, while it is pulled down by the $[1,0]$ transition after the phase boundary. This causes the boundary to appear to be shifted to higher values of y (or z if y is taken as fixed). There may also be an effect due to an unintended ZZ rotation, which is a well-known error for quantum computers built from fixed-frequency transmons [32,33]. While it is difficult to disentangle all of the sources of error, our goal is not to remove the error completely but to demonstrate the procedure for finding the phase boundary using our spectroscopic eigensolver. The accuracy is determined by the width of the dips, set by the time t for which the algorithm can run, which is limited by the number of quantum gates which can be applied before decoherence becomes large. As quantum hardware improves, this number of gates will increase, and the accuracy of our algorithm will improve.

While the energy transitions are symmetric between positive and negative values of m , it is often the case that a particular transition is more apparent in the data for either \pm values of m . Figure 4 is generated by taking the most accurate data between positive and negative m . For the raw data and a detailed discussion of how the data were filtered see Appendix E.

VI. CONCLUSION

The experiments discussed here demonstrate the ability of the spectroscopic eigensolver technique to solve for eigenspectra on near-term quantum devices. Similar to the experimental method of tunneling spectroscopy, the simulation register interacts with a local probe qubit to determine its spectrum. This requires only the realization of two-qubit interactions between the probe and register without the coherent control of the register at the heart of many other simulation algorithms, making this technique highly amenable to exploration on near-term noisy quantum computing hardware.

ACKNOWLEDGMENTS

The authors acknowledge the use of IBM Quantum Services for this work. The authors also thank C. S. Hellberg, L. D. Gunlycke, D. J. Egger, S. M. Frolov, P. Jurcevic, and Y. Kim for insightful discussions; D. T. McClure, P. Nation, S. Panda, and R. Woo for assistance in performing the experiments; and K. J. Ferris, O. T. Lanes, and K. J. Sung for careful readings of the manuscript. We acknowledge the Air Force Research Laboratory (AFRL) for providing additional quantum resources through its partnership with IBM. This

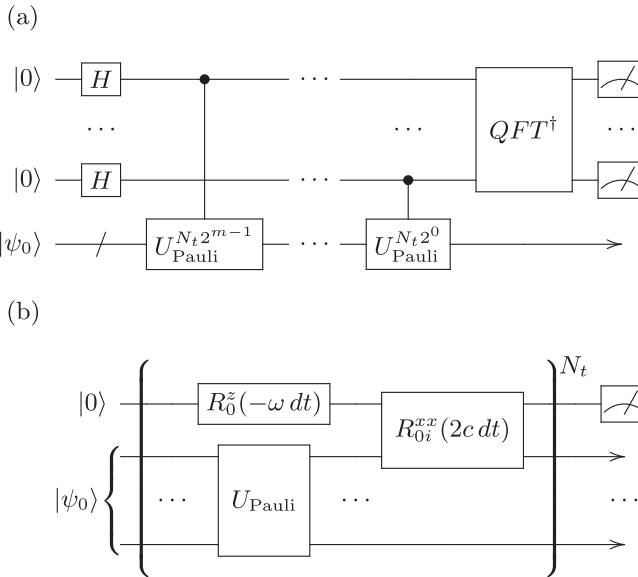


FIG. 5. Comparison of (a) QPE and (b) the spectroscopic eigensolver algorithms.

work has been supported by the Office of Naval Research (ONR) through the U.S. Naval Research Laboratory (NRL).

APPENDIX A: HAMILTONIAN SIMULATION ALGORITHMS

Quantum computers will theoretically give an exponential speedup to the problem of solving for the eigenvalues of Hamiltonians by the celebrated quantum phase estimation (QPE) algorithm [9]—the backbone of proposed universal quantum simulation [34]. QPE estimates the phase of a unitary operator U acting on an n -dimensional Hilbert space encoded by a “simulation” register to within an arbitrary precision specified by the number m of qubits in an auxiliary register. Performing QPE involves realizing controlled- U^k gates (Trotterized into N_t steps each) on n qubits (with $1 \leq k \leq 2^{m-1}$) followed by an inverse quantum Fourier transform on the auxiliary register [as depicted in Fig. 5(a)] and is prohibitive for near-term noisy quantum hardware [35]. Current research thrusts involve reducing the quantum resources necessary for performing quantum simulations while still seeking exponential speedup. One such method known as iterative phase estimation (IPE) replaces the m -qubit auxiliary register with a recycled “pointer” qubit via mid-circuit measurements and feedforward [36]. Another method involves performing a classical Fourier transform on the time series generated by expectation values of the phase kickback on the auxiliary qubit from a controlled U on the simulation register [37]. The spectroscopic eigensolver [see Fig. 5(b) for comparison], however, uses only a local interaction and does not require coherent control of the register to elucidate the eigenvalues. As a demonstration of the expected performance, we will estimate a fidelity score for the resource extremal case of QPE.

The accuracy of the spectroscopic eigensolver in the Landau-Zener model is approximately equivalent to three bits of precision ($\sim 10\%$) and is obtained with a single-qubit simulation register. The same precision in QPE requires a

TABLE I. A comparison of parameters between QPE and the spectroscopic eigensolver (Spec. Eigen.) for the Landau-Zener model and that implemented with $R^{zx}(\theta)$ operations, the count of which is denoted by an asterisk (*).

	QPE	Spec. Eigen.	Spec. Eigen. with R^{zx}
No. qubits	4	2	2
No. CNOTS	1272	120	60*
Infidelity score	0.99984	0.65363	0.06018

three-qubit measurement register. Using the PHASEESTIMATION circuit from QISKit with the same Trotterization, SWAP mapping determined by the (stochastic) SABRESWAP method of the QISKit transpiler, the resulting circuit is mapped to the least noisy qubits on IBM Lagos with the MAPOMATIC package [38]. The MAPOMATIC package provides an infidelity score calculated from single- and two-qubit gate error and measurement error, with each R^{zx} gate error calculated as linear in angle (as found in Ref. [2]) with a floor of the X error that forms the echo. These are reported in Table I. We see that QPE is estimated to have three-9’s of infidelity, while the spectroscopic eigensolver is around 65%, which improves to 6% when pulse-scaled R^{zx} gates are used. Note that while these exact values are based on current error rates determined by calibration and are subject to frequent change, they provide an estimate to the required quantum resources.

APPENDIX B: FUNCTIONAL FORM OF THE RESONANCE EIGENSOLVER

The algorithm works by applying unitary time evolution to an arbitrary state (in our simulation we choose $|\psi_0\rangle = |000\rangle$) of the system with the probe qubit in the ground state. We then observe the probability that the probe qubit becomes excited. If the energy on the probe qubit (as swept by ω in the resonance Hamiltonian, not the actual transition energy of the transmon as in [39]) matches an energy transition in the system, then we will find a peak in the probability. To demonstrate that the probability indeed peaks at energy transitions, we will use two approaches. First, we will derive the first-order perturbation of the probability as a function of probe qubit frequency. This will show us that the probability decays as the frequency of the probe qubit is taken off resonance. Second, we will analyze the behavior of the probability when the system is composed of only two energy levels. Since the probability decays away from resonance, a two-level system is a good approximation for a larger system where a particular transition is close to resonance with the probe qubit.

Let us start with the perturbation approach. In the algorithm, we apply unitary time evolution

$$U_{\text{res}}(\omega) = e^{-i(-\omega Z_0/2 + H_{\text{Pauli}} + cX_0 X_i)dt}, \quad (\text{B1})$$

where H_{Pauli} is the qubit-encoded system Hamiltonian, qubit 0 is the probe qubit, and qubit i is the qubit being probed. We desire c to be small so that we can treat the $cX_0 X_i$ term as a perturbation. Let E_n and $|n\rangle$ be the energies and eigenvectors of the system Hamiltonian H_{Pauli} $|n\rangle = E_n |n\rangle$ so that the unperturbed eigenvalues are $E_{a,n} = (-1)^{a+1}\omega/2 + E_n$ and the unperturbed eigenvectors are $|a,n\rangle$, where $a \in \{0, 1\}$ labels

the state of the probe qubit, i.e.,

$$\begin{aligned} \left(-\frac{1}{2}\omega Z_0 + H_{\text{Pauli}} \right) |a, n\rangle &= E_{a,n} |a, n\rangle \\ &= \left(\frac{(-1)^{a+1}}{2}\omega + E_n \right) |a, n\rangle. \end{aligned} \quad (\text{B2})$$

Let \bar{E}_{an} be the energy of the entire resonance Hamiltonian and $|\bar{a}n\rangle$ be the eigenvectors so that

$$\left(-\frac{1}{2}\omega Z_0 + H_{\text{Pauli}} + cX_0X_1 \right) |\bar{a}n\rangle = \bar{E}_{an} |\bar{a}n\rangle. \quad (\text{B3})$$

To first order in c we have

$$\begin{aligned} \bar{E}_{an} &\approx E_{an} + c \langle a, n | X_0X_1 | a, n \rangle = E_{an}, \\ |\bar{a}n\rangle &\approx |an\rangle + c \sum_{bm \neq an} |bm\rangle \frac{\langle bm | X_0X_1 | an \rangle}{E_{an} - E_{bm}}. \end{aligned} \quad (\text{B4})$$

The initial state of the algorithm has the probe qubit in the ground state and the system qubits in an arbitrary state. We are interested in the probability that the auxiliary qubit will flip regardless of the state of the system after time evolution. We can write the entire algorithm in one line,

$$\langle Z_0 \rangle (\omega) = 1 - 2 \sum_m \left| \sum_n \alpha_n \langle 1m | U_{\text{res}}(\omega)^{N_t} | 0n \rangle \right|^2, \quad (\text{B5})$$

where the parameters α_n are arbitrary, reflecting that we start in an arbitrary state of the system. To evaluate this probability, we need to evaluate

$$\begin{aligned} \langle 1m | \left(-\frac{1}{2}\omega Z_0 + H_S + cX_0X_1 \right)^l | 0n \rangle \\ = \sum_{ak} \langle 1m | \bar{a}k \rangle \langle \bar{a}k | 0n \rangle \bar{E}_{ak}^l, \end{aligned} \quad (\text{B6})$$

where l is any non-negative integer. To first order, we have

$$\langle 1m | \bar{a}k \rangle = \delta_{a1} \delta_{km} + c \frac{\chi_{mk}}{E_{0m} - E_{1k}} \delta_{a0}, \quad (\text{B7})$$

$$\langle \bar{a}k | 0n \rangle = \delta_{a0} \delta_{kn} + c \frac{\chi_{kn}}{E_{1k} - E_{0n}} \delta_{a1}, \quad (\text{B8})$$

where $\chi_{mn} = \langle m | X_1 | n \rangle$. We multiply these together and get

$$\begin{aligned} \langle 1m | \left(-\frac{1}{2}\omega Z_0 + H_S + cX_0X_1 \right)^l | 0n \rangle \\ = c \chi_{mn} \left(\frac{E_{1m}^l}{E_{1m} - E_{0n}} + \frac{E_{0n}^l}{E_{0m} - E_{1n}} \right). \end{aligned} \quad (\text{B9})$$

Now we can go back to the probability

$$\begin{aligned} \langle Z_0 \rangle (\omega) \\ = 1 - 2c^2 \left| \sum_{mn} \alpha_n \chi_{mn} \left(\frac{e^{iE_{1m}t}}{E_m - E_n + \omega} + \frac{e^{iE_{0n}t}}{E_m - E_n - \omega} \right) \right|^2. \end{aligned} \quad (\text{B10})$$

We see that the biggest contributions to the probability are the energies which are on resonance with the probe qubit. The

pole at $\omega = \pm(E_m - E_n)$ is unphysical since the perturbation is valid only for $c < E_m - E_n - \omega$ for all m and n .

To analyze the behavior near the resonance condition $\omega = \pm(E_1 - E_0)$, we can ignore the other energy levels since they do not contribute as strongly. In this case we are left with a two-level system. We can fully analytically analyze our algorithm for this two-level system, which will tell us generally the behavior of the algorithm when ω is near an energy transition. Let us write the two-level system Hamiltonian as

$$H_0 = \frac{1}{2}dZ_1, \quad (\text{B11})$$

where $d = E_1 - E_0$. The full Hamiltonian is

$$H = \frac{1}{2}\omega Z_0 + \frac{1}{2}dZ_1 + cX_0X_1. \quad (\text{B12})$$

This has eigenvalues

$$\begin{aligned} E_a^\pm &= \pm \frac{1}{2} \sqrt{4c^2 + (d - \omega)^2}, \\ E_b^\pm &= \pm \frac{1}{2} \sqrt{4c^2 + (d + \omega)^2} \end{aligned} \quad (\text{B13})$$

and eigenvectors

$$\begin{aligned} |a\pm\rangle &= \left(\frac{d - \omega + 2E_a^\pm}{2N_a^\pm} |01\rangle - \frac{c}{N_a^\pm} |10\rangle \right), \\ |b\pm\rangle &= \left(\frac{d + \omega + 2E_b^\pm}{2N_b^\pm} |00\rangle + \frac{c}{N_b^\pm} |11\rangle \right), \end{aligned} \quad (\text{B14})$$

where

$$\begin{aligned} N_a^\pm &= \frac{1}{\sqrt{2}} \sqrt{(d - \omega)^2 + 4c^2 - 2(d - \omega)E_a^\pm}, \\ N_b^\pm &= \frac{1}{\sqrt{2}} \sqrt{(d + \omega)^2 + 4c^2 + 2(d + \omega)E_b^\pm}. \end{aligned} \quad (\text{B15})$$

Thus, we can write time evolution as

$$\begin{aligned} e^{-iHt} &= e^{-iE_a^-} |a-\rangle \langle a-| + e^{-iE_a^+} |a+\rangle \langle a+| \\ &\quad + e^{-iE_b^-} |b-\rangle \langle b-| + e^{-iE_b^+} |b+\rangle \langle b+|. \end{aligned} \quad (\text{B16})$$

Using this form of the time-evolution operator, it is straightforward (although tedious) to derive the bracket,

$$\langle 1m | e^{iH(\omega)t} | 0n \rangle = A(\omega) \delta_{n1} \delta_{m0} + B(\omega) \delta_{n0} \delta_{m1}, \quad (\text{B17})$$

where

$$\begin{aligned} A(\omega, d) &= i \frac{2c}{\sqrt{4c^2 + (d - \omega)^2}} \sin(E_a t), \\ B(\omega, d) &= i \frac{2c}{\sqrt{4c^2 + (d + \omega)^2}} \sin(E_b t). \end{aligned} \quad (\text{B18})$$

Once again, we see that the probability is maximized when $\omega = \pm d$.

We use the functional form to assist in finding the minima in the data. Figure 6 shows the functional form fitted to the data from IBM Lagos. We begin the fitting by smoothing the data (averaging over the nearest four data points) and then finding the zeros in the derivative. We expect two energy transitions within the data range, specifically the [0,1] transition and the [2,3] transition, which are both small. If we find two

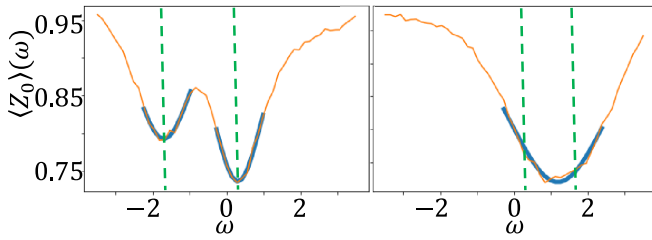


FIG. 6. Fit of the IBM Lagos data to the functional form. The orange curves are the experimental data, the blue curves are the fit, and the green dashed lines show the location of the transitions according to the fit.

zeros (left panel in Fig. 6), then we take the 10 nearest points to each minimum found by the derivative and separately fit them to $|A(\omega, d)|^2$. If we find only one minimum (right panel in Fig. 6), then we take the 20 nearest points and fit them to $|A(\omega, d1) + A(\omega, d2)|^2$. In other words, we expect that the two transitions are close enough that they form a single dip.

APPENDIX C: ZERO-ENERGY RESONANCE DIP

In Fig. 2 of the main text, we see a dip in $\langle Z_0 \rangle(\omega)$ at $\omega = 0$. However, this peak is absent in the Kitaev chain data. To understand the origin of the zero peak let us return to the function form of the probe qubit orientation as derived in Appendix B,

$$\langle Z_0 \rangle(\omega) = 1 - 2c^2 \left| \sum_{mn} \alpha_n \chi_{mn} \left(\frac{e^{iE_{1m}t}}{E_m - E_n + \omega} + \frac{e^{iE_{0n}t}}{E_m - E_n - \omega} \right) \right|^2. \quad (\text{C1})$$

We see that there is a dip in $\langle Z_0 \rangle(\omega)$ when $\omega = E_m - E_n$. Since the sum is over all m and n , we should expect a zero-energy dip for $m = n$ unless $\chi_{nn} = 0$. Recall that

$$\chi_{mn} = \langle m | X_1 | n \rangle, \quad (\text{C2})$$

which may not be zero depending on the eigenvectors $|n\rangle$ of the Hamiltonian. If, however, the Hamiltonian describes fermions and we are using the Jordan-Wigner transformation as in the main text, then X_1 creates or destroys a single fermion. Since fermion Hamiltonians conserve parity, they always have $\chi_{nn} = 0$. Therefore, we should not expect a zero dip for fermion Hamiltonians. If, however, there is some small error in term which couples the system to the probe when implemented on the quantum hardware, then a zero dip can show up. For this work we were careful to find qubits that did show a zero peak for the fermion model.

APPENDIX D: OPTIMIZATION

The coupling strength c between the probe qubit and the system, the total evolution time t , and the time step dt all need to be optimized for the algorithm. In Fig. 7 we see the orientation of the probe qubit as a function of both ω and c . We want to focus on the ground to first excited state transition labeled [0,1]. We see that when $c > 0.5$, the dip corresponding to the [0,1] transition is shifted due to the large

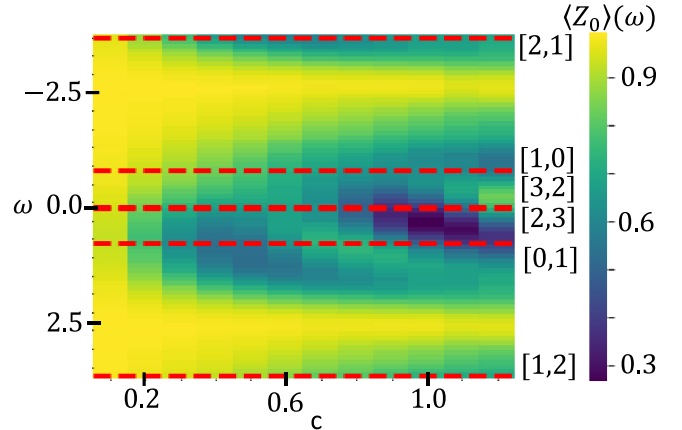


FIG. 7. Expectation values of the Z component of the probe qubit as a function of ω and c . The other parameters are set to $x = 1.5$, $y = 0.4$, $z = -0.3$, $t = 5.0$, and $dt = 1.2$. The dashed red lines show the location of the energy transitions. The lines are labeled on the right by the two states involved in the transition; for example, [0,1] is the transition from state 0 to state 1.

interaction between the probe and the system, and in fact, the reverse transition [1,0] and higher-order transitions [2,3] and [3,2] also appear (but also shifted) at these strong coupling values. However, for $c < 0.1$ the dip is washed out. We choose $c = 0.3$, where the dip corresponding to the correct transition ([0,1]) is apparent and at the correct value, and no other nearby transitions are observed.

Once the optimum c value was found, we optimized time step dt and total time t in a similar way. Then we reoptimized c at the new values of t and dt and found that the optimum c value had not changed. Figure 8 shows the Z expectation of the probe qubit as a function of ω and t for two values of dt . We see that if t is too short, the dip is washed out just like for small c . Additionally, if dt is too small, then we run into errors due to the increased number of gates that are applied to the quantum register. We want the smallest dt we can manage so that our Suzuki-Trotter decomposition is as accurate as possible.

Informed by these optimization experiments and others, we chose the parameter set $t = 5.0$, $dt = 0.7$, and $c = 0.3$ for this

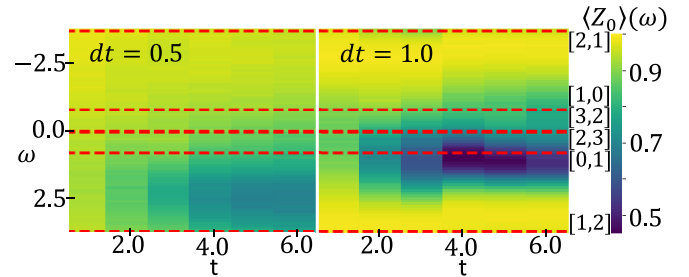


FIG. 8. Expectation values of the Z component of the probe qubit as a function of ω and t for $dt = 0.5$ (left) and $dt = 1.0$ (right). The other parameters are set to $x = 1.5$, $y = 0.4$, $z = -0.3$, and $t = 0.4$. The dashed red lines show the location of the energy transitions. The lines are labeled on the right by the two states involved in the transition; for example, [0,1] is the transition from state 0 to state 1.

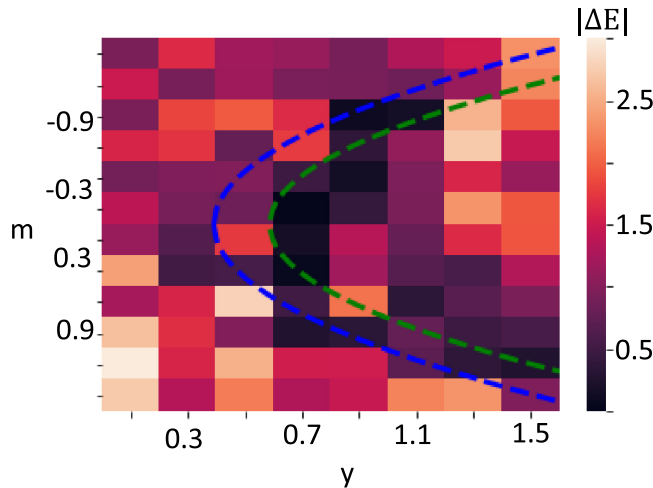


FIG. 9. The raw data of the energy gap as a function of m and y . The parameter values match those in Fig. 4 of the main text. The dashed blue curve shows the location of the phase transition calculated from Eq. (6) of the main text, while the green curve is a best fit of the data to Eq. (6) using z as the fit parameter.

work. More data were analyzed than those presented here, and we have made our full data set accessible on GitHub [22].

APPENDIX E: APPLYING THE CHEMICAL POTENTIAL SYMMETRY

We know that the energy spectrum is symmetric about $m \rightarrow -m$. Therefore, if we know the zero-crossing phase boundary for $+m$, we can infer the phase boundary for $-m$ and vice versa. Figure 9 shows the raw data for the energy gap as a function of m and y . In the main text we selected the smallest gap between positive and negative m to be the gap for both. In this way, we filter out the data in which the $[0,1]$ transition has been washed out by the $[2,3]$ transition. Sometimes the $[2,3]$ transition has a much larger response than the $[0,1]$ transition. When this happens the $[2,3]$ transition can wash out the $[0,1]$ transition, so that the fitting technique fails to provide an accurate estimate of the $[0,1]$ transition. Thus, we get more accurate data by selecting between the transitions at positive and negative m . We find that the zero crossing of the $[0,1]$ transition is easily extractable from the data for negative m in the range of $0.7 \leq y \leq 1.1$, while for $1.1 < y$ the positive m values show the $[0,1]$ zero crossing clearly.

APPENDIX F: APPROACHING THE $n \rightarrow \infty$ LIMIT IN THE KITAEV CHAIN

We can approach the $L \rightarrow \infty$ limit by increasing the number of sites. In Fig. 10 we plot maps of the energy gap for different values of L . The parameters are set to $x = 1.5$, $z = \bar{m} = 0.4$. For $L > 2$, we see that the gap opens and closes multiple times. The larger L is, the more the gap closes, and the smaller the peaks are between the lines where the gap closes. In this way, one could approach the case where the gap stays closed.

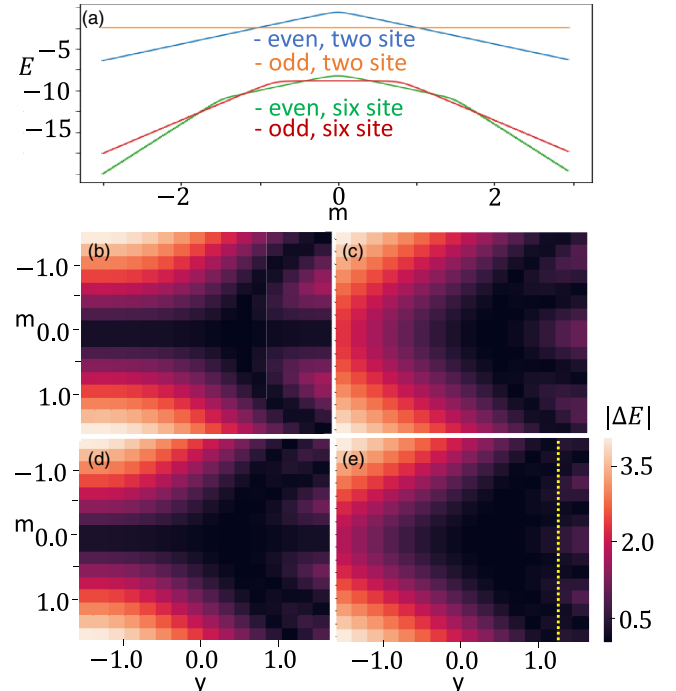


FIG. 10. Energy gap for increasing chain length. The plots are generated from a classical simulation. In (a) we plot the (absolute) energy of the lowest even and lowest odd parity states versus m for two sites and for six sites at $y = 1.3$ [m and y are defined in Eq. (6)]. In the other panels, the energy gap between the lowest even and lowest odd parity states is plotted against the parameters m and y . The points where $|\Delta E|$ goes to zero correspond to the crossing of the two lowest energy levels. Each plot has a different number of sites: (b) three sites, (c) four sites, (d) five sites, and (e) six sites; the dotted yellow line shows the location ($y = 1.3$) of the six-site energy cuts in (a). For a plot of the simulated two-site model, see Fig. 4(a).

APPENDIX G: TWO-SITE PARITY-FLIPPING BOUNDARY

In the main text we stated that the parity of the ground state changes along the boundary

$$m = \sqrt{z^2 + z(x+y) + xy} \quad (G1)$$

for the two-site Kitaev chain. This comes simply from diagonalizing the two-site Hamiltonian

$$H = mZ_1 + mZ_2 + xX_1X_2 + yY_1Y_2 + zZ_1Z_2, \quad (G2)$$

which has eigenvalues

$$\begin{aligned} E_a^\pm &= -z \pm (x+y), \\ E_b^\pm &= z \pm \sqrt{4m^2 + (x-y)^2}. \end{aligned} \quad (G3)$$

In the parameter regime of interest, E_a^- and E_b^- are the two lowest energy levels. We want to know when the ground state switches from E_a^- to E_b^- . Setting $E_a^- = E_b^-$ and solving for m gives the desired equation.

APPENDIX H: THREE-SITE MODEL DATA

We ran the spectroscopic algorithm for a three-site Kitaev chain. While the data are very accurate at certain parameter

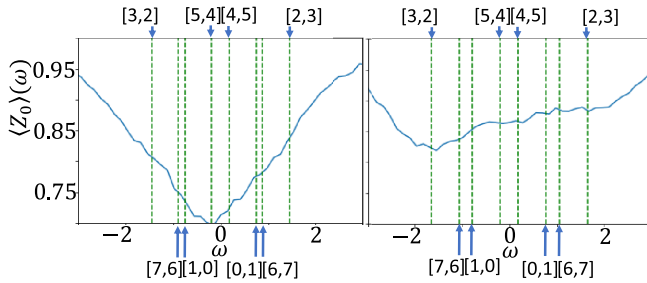


FIG. 11. Expectation of the Z component of the probe qubit as a function of ω for a three-site Kitaev chain. Left: $m = 0.5$. Right: $m = -0.5$. The other parameters are set to $x = 1.5$, $y = 1.1$, $z = 0.4$, $c = 0.3$, $dt = 0.7$, and $t = 5$. The green dashed lines show the energy transitions, which are labeled at the top and bottom of the plot.

values, we were not able to map out the full phase diagram. One issue is that the number of small-energy transitions increases, causing the width of the dips in $\langle Z_0 \rangle(\omega)$ to often absorb several of the weaker transitions. In Fig. 11 we plot $\langle Z_0 \rangle(\omega)$ for $m = 0.5$ (left) and $m = -0.5$ (right). While the energy transitions are symmetric in m , the algorithm often favors different transitions for positive and negative m . In this case, the [5,4] transition is favored for positive m , while [3,2] is favored for negative m . While this asymmetry in the favored transition is present for the two-site case as well, there we were able to resolve the secondary transition for many param-

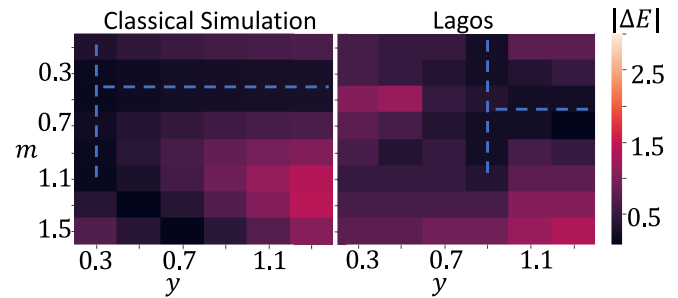


FIG. 12. The [5,4] energy transition as a function of y and m . Left: from directly solving for the eigenvalues of the Hamiltonian. Right: from the spectroscopic algorithm run on Lagos. The other parameters are set to $x = 1.5$, $z = 0.4$, $c = 0.3$, $dt = 0.7$, and $t = 5$.

eter values. For the three-site model, the secondary transitions are very difficult to resolve, if they are present at all.

Still, we are able to trace out the zero crossings for certain energy transitions for a range of parameters. Figure 12 shows the zero crossing for the [5,4] transition in a small range of m and y . While the transition is shifted just like in the two-site case, the main features are present. The data could be improved by narrowing the dips in $\langle Z_0 \rangle(\omega)$. A possible solution for narrowing the dips would be to increase t , which for this work was limited by qubit coherence and classical wave form generation bandwidth for IBM Lagos. It is expected that future generations of superconducting quantum backends will allow for such exploration.

-
- [1] R. P. Feynman, Simulating physics with computers, *Int. J. Theor. Phys.* **21**, 467 (1982).
 - [2] J. P. T. Stenger, N. T. Bronn, D. J. Egger, and D. Pekker, Simulating the dynamics of braiding of Majorana zero modes using an IBM quantum computer, *Phys. Rev. Res.* **3**, 033171 (2021).
 - [3] X. Xiao, J. K. Freericks, and A. F. Kemper, Determining quantum phase diagrams of topological Kitaev-inspired models on NISQ quantum hardware, *Quantum* **5**, 553 (2021).
 - [4] M. J. Rančić, Exact solution and Majorana zero mode generation on a Kitaev chain composed out of noisy qubits, [arXiv:2108.07235](https://arxiv.org/abs/2108.07235).
 - [5] K. J. Sung, M. J. Rančić, O. T. Lanes, and N. T. Bronn, Preparing Majorana zero modes on a noisy quantum processor, [arXiv:2206.00563](https://arxiv.org/abs/2206.00563).
 - [6] N. Harle, O. Shtanko, and R. Movassagh, Observing and braiding topological Majorana modes on programmable quantum simulators, [arXiv:2203.15083](https://arxiv.org/abs/2203.15083).
 - [7] X. Mi *et al.*, Noise-resilient Majorana edge modes on a chain of superconducting qubits, [arXiv:2204.11372](https://arxiv.org/abs/2204.11372).
 - [8] Y. Kim, C. J. Wood, T. J. Yoder, S. T. Merkel, J. M. Gambetta, K. Temme, and A. Kandala, Scalable error mitigation for noisy quantum circuits produces competitive expectation values, [arXiv:2108.09197](https://arxiv.org/abs/2108.09197).
 - [9] A. Y. Kitaev, Quantum measurements and the Abelian stabilizer problem, [arXiv:quant-ph/9511026](https://arxiv.org/abs/quant-ph/9511026).
 - [10] A. Peruzzo, J. McClean, P. Shadbolt, M.-H. Yung, X.-Q. Zhou, P. J. Love, A. Aspuru-Guzik, and J. L. O'Brien, A variational eigenvalue solver on a photonic quantum processor, *Nat. Commun.* **5**, 4213 (2014).
 - [11] A. Kandala, A. Mezzacapo, K. Temme, M. Takita, M. Brink, J. M. Chow, and J. M. Gambetta, Hardware-efficient variational quantum eigensolver for small molecules and quantum magnets, *Nature (London)* **549**, 242 (2017).
 - [12] J. R. McClean, J. Romero, R. Babbush, and A. Aspuru-Guzik, The theory of variational hybrid quantum-classical algorithms, *New J. Phys.* **18**, 023023 (2016).
 - [13] P. J. J. O'Malley *et al.*, Scalable Quantum Simulation of Molecular Energies, *Phys. Rev. X* **6**, 031007 (2016).
 - [14] D. Wang, O. Higgott, and S. Brierley, Accelerated Variational Quantum Eigensolver, *Phys. Rev. Lett.* **122**, 140504 (2019).
 - [15] J. F. Gonthier, M. D. Radin, C. Buda, E. J. Doskocil, C. M. Abuan, and J. Romero, Measurements as a roadblock to near-term practical quantum advantage in chemistry: Resource analysis, *Phys. Rev. Res.* **4**, 033154 (2022).
 - [16] S. McArdle, S. Endo, A. Aspuru-Guzik, S. C. Benjamin, and X. Yuan, Quantum computational chemistry, *Rev. Mod. Phys.* **92**, 015003 (2020).
 - [17] R. Somma, G. Ortiz, J. E. Gubernatis, E. Knill, and R. Laflamme, Simulating physical phenomena by quantum networks, *Phys. Rev. A* **65**, 042323 (2002).
 - [18] A. Wack, H. Paik, A. Javadi-Abhari, P. Jurcevic, I. Faro, J. M. Gambetta, and B. R. Johnson, Quality, Speed, and Scale: Three

- key attributes to measure the performance of near-term quantum computers, [arXiv:2110.14108](https://arxiv.org/abs/2110.14108).
- [19] QISKit: An open-source framework for quantum computing, qiskit.org (2021).
 - [20] S. Sheldon, E. Magesan, J. M. Chow, and J. M. Gambetta, Procedure for systematically tuning up cross-talk in the cross-resonance gate, *Phys. Rev. A* **93**, 060302(R) (2016).
 - [21] R. Iten, R. Moyer, T. Metger, D. Sutter, and S. Woerner, Exact and practical pattern matching for quantum circuit optimization, [arXiv:1909.05270](https://arxiv.org/abs/1909.05270).
 - [22] Qiskit Research, <https://www.github.com/qiskit-research/qiskit-research>.
 - [23] A. Y. Kitaev, Fault-tolerant quantum computation by anyons, *Ann. Phys. (NY)* **303**, 2 (2003).
 - [24] C. Nayak, S. H. Simon, A. Stern, M. Freedman, and S. S. Das Sarma, Non-Abelian anyons and topological quantum computation, *Rev. Mod. Phys.* **80**, 1083 (2008).
 - [25] J. Alicea, Y. Oreg, G. Refael, F. von Oppen, and M. P. A. Fisher, Non-Abelian statistics and topological quantum information processing in 1D wire networks, *Nat. Phys.* **7**, 412 (2011).
 - [26] P. Bonderson and R. M. Lutchyn, Topological Quantum Buses: Coherent Quantum Information Transfer between Topological and Conventional Qubits, *Phys. Rev. Lett.* **106**, 130505 (2011).
 - [27] J. P. T. Stenger, M. Hatridge, S. M. Frolov, and D. Pekker, Braiding quantum circuit based on the 4π Josephson effect, *Phys. Rev. B* **99**, 035307 (2019).
 - [28] G. Ben-Shach, A. Haim, I. Appelbaum, Y. Oreg, A. Yacoby, and B. I. Halperin, Detecting Majorana modes in one-dimensional wires by charge sensing, *Phys. Rev. B* **91**, 045403 (2015).
 - [29] A. M. Childs, D. Maslov, Y. Nam, N. J. Ross, and Y. Su, Toward the first quantum simulation with quantum speedup, *Proc. Natl. Acad. Sci. USA* **115**, 9456 (2018).
 - [30] F. Tacchino, A. Chiesa, S. Carretta, and D. Gerace, Quantum computers as universal quantum simulators: State-of-the-art and perspectives, *Adv. Quantum Technol.* **3**, 1900052 (2020).
 - [31] J. Chen, P. Yu, J. Stenger, M. Hocevar, D. Car, S. R. Plissard, E. P. A. M. Bakkers, T. D. Stanescu, and S. M. Frolov, Experimental phase diagram of zero-bias conductance peaks in superconductor/semiconductor nanowire devices, *Sci. Adv.* **3**, e1701476 (2017).
 - [32] A. Kandala, K. X. Wei, S. Srinivasan, E. Magesan, S. Carnevale, G. A. Keefe, D. Klaus, O. Dial, and D. C. McKay, Demonstration of a High-Fidelity CNOT for Fixed-Frequency Transmons with Engineered ZZ Suppression, *Phys. Rev. Lett.* **127**, 130501 (2021).
 - [33] N. Sundaresan, I. Lauer, E. Pritchett, E. Magesan, P. Jurcevic, and J. M. Gambetta, Reducing unitary and spectator errors in cross resonance with optimized rotary echoes, *PRX Quantum* **1**, 020318 (2020).
 - [34] S. Lloyd, Universal quantum simulators, *Science* **273**, 1073 (1996).
 - [35] J. Preskill, Quantum computing in the NISQ era and beyond, *Quantum* **2**, 79 (2018).
 - [36] A. D. Córcoles, M. Takita, K. Inoue, S. Lekuch, Z. K. Minev, J. M. Chow, and J. M. Gambetta, Exploiting Dynamic Quantum Circuits in a Quantum Algorithm with Superconducting Qubits, *Phys. Rev. Lett.* **127**, 100501 (2021).
 - [37] R. D. Somma, Quantum eigenvalue estimation via time series analysis, *New J. Phys.* **21**, 123025 (2019).
 - [38] MAPOMATIC: Automatic mapping of compiled circuits to low-noise sub-graphs, <https://github.com/Qiskit-Partners/mapomatic>.
 - [39] P. Roushan *et al.*, Spectroscopic signatures of localization with interacting photons in superconducting qubits, *Science* **358**, 1175 (2017).